







The role of aromaticity in the cyclization and polymerization of alkyne-substituted porphyrins on Au(111)

Nan Cao ¹, Jonas Björk ², Eduardo Corral-Rascon¹, Zhi Chen ^{3,4}, Mario Ruben ^{3,5,6}, Mathias O. Senge ⁷, Johannes V. Barth ¹✉ & Alexander Riss ¹✉

Aromaticity is an established and widely used concept for the prediction of the reactivity of organic molecules. However, its role remains largely unexplored in on-surface chemistry, where the interaction with the substrate can alter the electronic and geometric structure of the adsorbates. Here we investigate how aromaticity affects the reactivity of alkyne-substituted porphyrin molecules in cyclization and coupling reactions on a Au(111) surface. We examine and quantify the regioselectivity in the reactions by scanning tunnelling microscopy and bond-resolved atomic force microscopy at the single-molecule level. Our experiments show a substantially lower reactivity of carbon atoms that are stabilized by the aromatic diaza[18]annulene pathway of free-base porphyrins. The results are corroborated by density functional theory calculations, which show a direct correlation between aromaticity and thermodynamic stability of the reaction products. These insights are helpful to understand, and in turn design, reactions with aromatic species in on-surface chemistry and heterogeneous catalysis.

Aromaticity is one of the most practical and versatile concepts for the assessment of the reactivity of organic compounds^{1,2}. The International Union of Pure and Applied Chemistry highlights three criteria for aromaticity³: (1) an energetic criterion describing the increased thermodynamic stability of the compounds, (2) a magnetic criterion associated with diamagnetic ring currents when the molecules are placed in an external magnetic field, and (3) a structural criterion based on the bond length alteration of the conjugated bonds; instead of alternating longer C–C single bonds and shorter C=C double bonds, in aromatic systems uniform bond lengths are approached (with values between the single and double bond lengths).

Hückel derived a quantum mechanical explanation for the aromatic stabilization of ring systems that exhibit $[4n + 2]$ π -electrons, such as benzene⁴. This rule also explained the aromatic character of the negatively charged cyclopentadienyl anion $[\text{C}_5\text{H}_5]^-$, as well as the positively charged cycloheptatrienyl cation $[\text{C}_7\text{H}_7]^+$, both of which contain six π -electrons. Analogously, the rule was applied to heterocycles. For instance, the aromatic five-membered furan ($\text{C}_4\text{H}_4\text{O}$) and pyrrole ($\text{C}_4\text{H}_4\text{NH}$) rings both contain six π -electrons.

The situation is more intricate for macrocyclic systems, such as porphyrins, where four pyrrole rings are connected by methine bridges ($=\text{CH}-$). As shown in Fig. 1, free-base porphyrins (that is, porphyrins

¹Physics Department E20, Technical University of Munich, Garching, Germany. ²Department of Physics, Chemistry and Biology, IFM, Linköping University, Linköping, Sweden. ³Institute of Nanotechnology, Karlsruhe Institute of Technology, Eggenstein-Leopoldshafen, Germany. ⁴College of Chemistry and Environmental Engineering, Shenzhen University, Shenzhen, PR China. ⁵Centre Européen de Science Quantique, Institut de Science et d'Ingénierie Supramoléculaires (UMR 7006), CNRS-Université de Strasbourg, Strasbourg, France. ⁶Institute of Quantum Materials and Technologies, Karlsruhe Institute of Technology, Eggenstein-Leopoldshafen, Germany. ⁷Institute for Advanced Study (TUM-IAS), Focus Group—Molecular and Interfacial Engineering of Organic Nanosystems, Technical University of Munich, Garching, Germany. ✉e-mail: jvb@tum.de; a.riss@tum.de

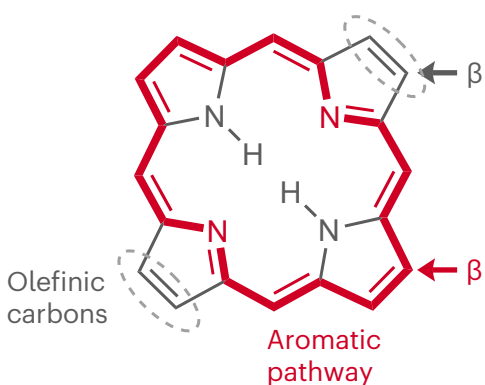


Fig. 1 | Aromaticity-driven regioselectivity in free-base porphyrins. The aromatic 18 π -electron diaza[18]annulene pathway (red highlighted bonds) along the macrocycle of a free-base porphyrin omits four carbon atoms. Thus, there are two chemically different types of carbon atoms at the β positions: carbons with aromatic character and carbons with olefinic (that is, double-bond) character⁵⁻⁷.

containing two hydrogen atoms instead of a metal atom in the centre) exhibit an aromatic diaza[18]annulene pathway with 18 π -electrons⁵⁻⁸. This pathway, which omits four of the peripheral carbon atoms, is reflected in the nuclear magnetic spectroscopy characteristics^{9,10}, and, importantly, has important implications for the chemical reactivity of porphyrins: the omitted pairs of carbon atoms at opposite ‘corners’ of the porphyrin exhibit olefinic character and are substantially more reactive towards addition reactions^{11,12}.

In on-surface chemistry, aromaticity is prominently discussed in the context of the synthesis of antiaromatic molecules¹³⁻¹⁸, as well as in recent work that qualitatively investigates how different charge states of aromatic molecules can affect specific bond lengths¹⁹. However, the connection between aromaticity and on-surface reactivity of organic molecules remains largely unexplored. While various reactions of (polycyclic) aromatic molecules²⁰⁻²² and, in particular, coupling of porphyrins²³⁻³¹, have been studied on surfaces, none of these studies identifies the role of aromaticity in the reactions. Recent investigations report differences in the reactivity of functional groups depending on whether these groups are linked to an aromatic ring system^{32,33}. The effect of aromaticity, however, was not quantified in these studies, nor were the aromatic moieties directly involved in the reaction (instead, the reaction took place at substituents connected to an aromatic system). Moreover, it is expected that a substantial change of the reactant will affect a variety of other parameters, such as the steric effects, the electronic interaction with the substrate, and charge transfer. Such effects are particularly relevant on metal surfaces, where electronic hybridization, fractional charge transfer and the geometric confinement of the molecules can substantially alter the thermodynamics and kinetics of the reaction^{22,34}.

In this Article, we show how aromaticity affects the on-surface reactivity of alkyne-substituted free-base porphyrins that undergo cyclization and coupling reactions on a Au(111) substrate. We compared the reactivity of the aromatic versus olefinic carbon atoms at the β positions (that is, at the ‘corners’) of the molecules (Fig. 1). As these carbons atoms are in structurally equivalent environments, the effect of aromaticity on the regioselectivity of the reactions can be discriminated from other parameters (such as steric effects). We used scanning tunnelling microscopy (STM) and bond-resolved atomic force microscopy (AFM) to identify the precise atomic-scale structure of the reaction products and determined their relative abundances based on statistics using single-molecule counting. We find that the olefinic carbon atoms are more than five times more likely to participate in intramolecular cyclization reactions. This behaviour is corroborated by extensive density functional theory (DFT) calculations. The thermodynamic stability of the reaction products shows a direct correlation with

the molecular aromaticity (quantified on the basis of the bond length alteration along the aromatic pathways). Similarly, the activation barriers for cyclization are lower for the olefinic β -carbons, facilitating kinetic reaction control. Our results reveal that the aromaticity of porphyrins is preserved upon adsorption on the metal substrate and sensibly influences their reactivity.

Results and discussion

Cyclization and coupling of alkyne-substituted porphyrins

We used free-base porphyrins with alkyne substituents on two opposite *meso*-positions as precursors: 5,15-*bis*((trimethylsilyl)ethynyl)porphyrin, denoted as **1a** (see the chemical structure in Fig. 2a). To prevent polymerization in the crucible during thermal sublimation, the alkyne groups were protected with trimethylsilyl groups (-SiMe₃). Deposition of **1a** on a Au(111) substrate kept at room temperature lead to the formation of small self-assembled islands co-existing with few isolated species (Fig. 2c). The molecules appear rod-like with bright spots at the two termini, assigned to the bulky -SiMe₃ groups (see also Supplementary Fig. 1).

Annealing the substrate at 305 °C induced a chemical transformation affording extended one-dimensional nanostructures with lengths commonly exceeding 30 units (Fig. 2d). The predominant products were chains with mostly regular arrangements of porphyrin constituents forming straight as well as angled connections, with few branching points (see also Supplementary Fig. 2). Some of the structures formed closed loops, that is, nanorings, typically consisting of five to six units. Additionally, we observed that almost all of the bright features associated with -SiMe₃ groups disappeared and only very few putative -SiMe₃ remnants remained on the surface (see dashed orange circles in Figs. 2d and 3a). We thus conclude that the -SiMe₃ groups cleaved off and largely desorbed upon annealing, in agreement with previous studies^{35,36} (see also Supplementary Fig. 2).

To clarify the connection motifs between porphyrin units, we performed bond-resolved AFM measurements with CO-functionalized tips³⁷. The AFM images of the polymeric structures (Fig. 3) indicate covalent connections between the porphyrin units with centre-to-centre distances of 1.10–1.20 nm. Furthermore, the images reveal the formation of new five-membered rings at the periphery of the porphyrins. Both reactions appear to be facilitated by the cleavage of the -SiMe₃ group, which exposes a reactive carbon atom; this atom then participates in the formation of two new C–C bonds associated with coupling and cyclization (Fig. 2a).

For the coupling reaction, we observe two different reaction pathways. These lead to (*Z*)- and (*E*)-type stereoisomers, which are defined with respect to the orientation of two neighbouring porphyrin units about the connecting C–C bond (Fig. 2b). Figure 3b shows a high-resolution image of a fragment composed of four porphyrin units showing both, (*E*)- and (*Z*)-type coupling. The coupling type is directly related to the morphologies formed: straight segments imply (*E*)-coupling, while (*Z*)-coupled sequences entail curved and ring-like structures. Our experiments show that (*Z*)-coupling is slightly more common than (*E*)-coupling (Fig. 3d).

The additional rings at the periphery of the porphyrins originate from cyclization reactions of the ethynyl residues^{22,38}. In the vast majority of cases (>95%), five-membered rings are formed (see also Supplementary Fig. 4). The relative position of the two formed rings at both sides of the porphyrin lead to different isomers: *cis*- and *trans*-isomers. These are associated with the regioselectivity of the cyclization reactions, that is, which β -pyrrole carbons the reactive ethynyl carbon atoms connect to (Fig. 2b). The high-resolution images (Fig. 3b,c) further reveal an increased brightness for some of the five-membered rings. This is probably caused by geometric distortions³⁹⁻⁴¹ and in some cases might be related to the degree of saturation at the specific carbon atoms, that is, extra hydrogen atoms pointing away from the surface³⁴ (see also Supplementary Figs. 7 and 20).

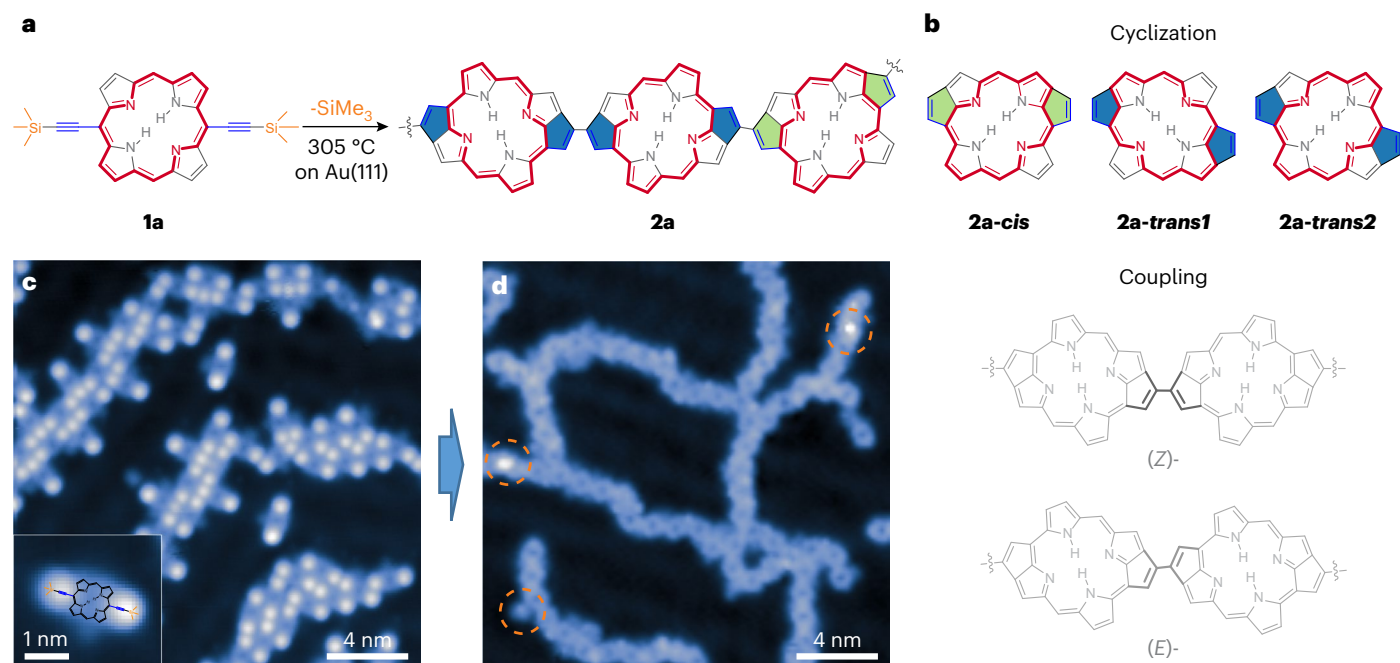


Fig. 2 | Cyclization and coupling of alkyne-substituted free-base porphyrins on Au(111). **a**, Reaction scheme of the transformation of the SiMe_3 -alkyne-substituted porphyrin precursor **1a** into covalently coupled one-dimensional porphyrin nanostructures **2a**. Thermally induced cleavage of the $-\text{SiMe}_3$ group exposes a reactive carbon atom, which participates in the formation of two new C–C bonds, leading to: (i) intramolecular cyclization to cyclopenta[*at*]porphyrin units via formation of five-membered rings (highlighted by green and blue fill colour), and (ii) intermolecular coupling. **b**, Chemical structures of the resulting reaction products, representing different isomeric configurations arising from the cyclization reactions (**2a-cis**, **2a-trans1** and **2a-trans2**) and the coupling

reactions ((*Z*)- and (*E*)-). The bold red highlight in the chemical models denotes the aromatic 18 π -electron diaza[18]annulene pathway observed in free-base porphyrins^{5–7}. **c**, STM image of the precursor **1a** after deposition on a Au(111) substrate held at room temperature shows self-assembled structures. The inset shows an isolated molecule with two protrusions at the positions of the $-\text{SiMe}_3$ groups. **d**, Upon annealing at 305 °C, STM shows the formation of covalently linked porphyrin nanostructures (**2a**), that is, chains and ring-like elements, via cyclization and coupling. Dashed orange circles mark bright spots that are probably associated with $-\text{SiMe}_3$ remnants. Scan parameters: $I_t = 10$ pA, $V_s = 50$ mV (**c**) and $I_t = 2$ pA, $V_s = 50$ mV (**d**).

Regioselectivity of the cyclization reaction

Statistical analysis of more than 200 molecules (Fig. 3d) reveals that *trans*-cyclization occurred much more frequently than *cis*-cyclization: 85% of molecules were found to be in *trans*-configuration, compared with 15% of *cis*-cyclized molecules (estimated error of $\pm 3\%$). The preference for *trans*-cyclization was not dependent on whether the molecules were coupled or isolated: analysis of more than 50 isolated molecules (about 3% of molecules remained isolated; Supplementary Fig. 3) similarly gave a four times higher abundance of *trans*-cyclized species. Based on the contrast in the AFM images, as well as tip-manipulation experiments, we determined that the all or almost all *trans*-cyclized species are of type **2a-trans2** (Fig. 3, Extended Data Figs. 1 and 2, and Supplementary Figs. 5 and 6; for a discussion on tautomerization effects, see Supplementary Fig. 5).

To understand the origin of this regioselectivity, we studied the energetics of the cyclization reaction by DFT calculations. In particular, we determined reaction energies for the three possible transformation pathways, that is, the energy differences between the reactant molecule (**1a**) and the three possible products (**2a-cis**, **2a-trans1** and **2a-trans2**) adsorbed on Au(111). We modelled **1a** as an alkyne-substituted porphyrin (that is, without the $-\text{SiMe}_3$ groups), such that the transformation does not entail any change of the number of atoms and the respective energies of the relaxed systems can be compared with each other. A different choice for the model of **1a** would not change any of the conclusions below, as we compare the products with each other (with respect to the reference point of **1a**).

The most stable adsorption configurations of the reactant and each of the three possible cyclization products are shown in Fig. 4a. The two *trans*-cyclized products, **2a-trans1** and **2a-trans2**, are different

N–H tautomers: despite their otherwise equal chemical structure, the different positions of the inner hydrogen atoms cause a different optimal adsorption position on the substrate and, importantly, influence the aromatic pathway (to be discussed in detail below). While other hydrogen tautomer configurations are conceivable^{42,43}, we have restricted our calculations to the most common scenario of tautomers, in which the inner hydrogens are in opposite positions^{44–49}. For the *cis*-cyclized product (**2a-cis**), as well as for the reactant **1a**, different hydrogen tautomers can be seen as mirror images of each other and, thus, are equivalent.

The DFT simulations reveal that **2a-trans2** is the energetically most favourable product ($\Delta E = -2.17$ eV), followed by **2a-cis** ($\Delta E = -2.04$ eV) and **2a-trans1** ($\Delta E = -2.01$ eV). This trend is still valid if the respective molecules occupy different adsorption sites, which might be the case for the porphyrin units within the chains (see below and Extended Data Fig. 3). The calculated energy differences directly explain why *cis*-cyclized species were less commonly observed in our experiments. However, since all the reaction pathways are exothermic with reaction energies differences of less than 0.2 eV, co-existence of the different products is predicted (for an estimation of relative abundances of reaction products, see Supplementary Fig. 18). This agrees with our experimental observations showing a co-existence of *cis*- and *trans*-cyclized species. The calculations furthermore suggest that the **2a-trans2** tautomer is more common, in agreement with the experimental assignments.

Effect of aromaticity

These findings can be interpreted in the chemical framework of aromaticity. The aromatic pathway in free-base porphyrins (diaza[18]

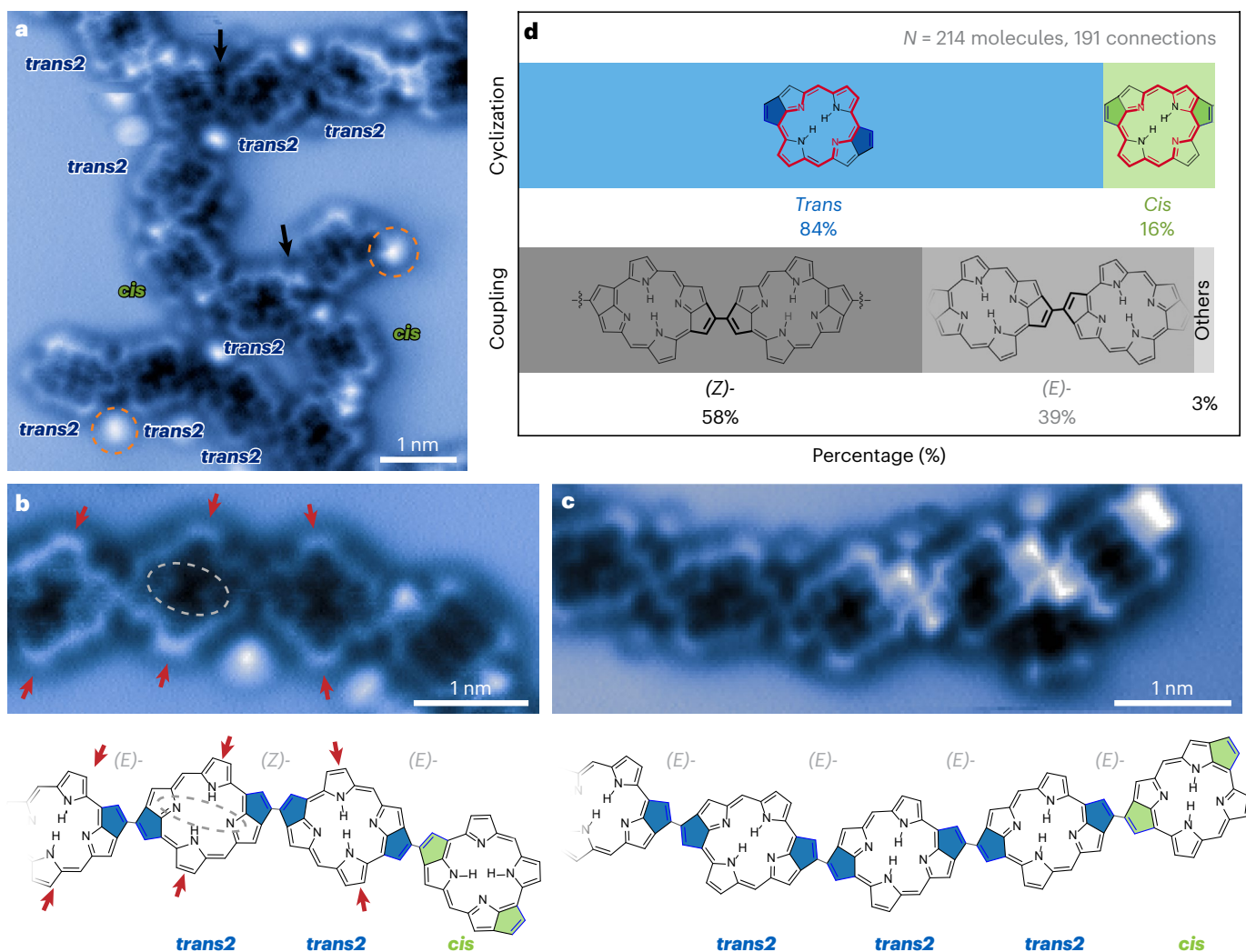


Fig. 3 | Regio- and stereoselectivity of cyclization and coupling reactions. **a**, Bond-resolved AFM image shows covalently coupled porphyrin nanostructures (**2a**), exhibiting regular segments and few irregular coupling motifs that gives rise to branch-like structures. Bright spots near the molecules (indicated by dashed orange circles) are probably related to remnants of $-\text{SiMe}_3$ or small adsorbed molecules (such as CO). **b,c**, High-resolution AFM images of two different chain segments and their corresponding chemical structures highlight the isomeric reaction products for coupling, that is, (Z)- and (E)-, as well as for cyclization, that is, *cis* and *trans*. Brighter features at larger tip heights

indicate that the *trans*-species are of type **2a-trans2** (Extended Data Fig. 1). Similar features can also be seen at the tip height shown here: the dashed grey ellipse marks brighter features inside the macrocycle associated with the iminic nitrogens. Red arrows mark aminic pyrroles. **d**, Statistical analysis provides insights into the distribution of reaction product isomers for coupling and cyclization: Intramolecular cyclization shows a strong preference for *trans* products, while intermolecular coupling exhibits a more balanced yield of (Z)- and (E)-coupled products. Scan parameters: $V_s = 0$ V, constant height.

annulene with 18 π -electrons, red-coloured bonds in Figs. 2b and 4a) does not include all atoms in the macrocycle, but instead omits two $\text{C}_\beta=\text{C}_\beta$ units at opposite 'corners' (cf. Fig. 1). Due to the olefinic character and the increased reactivity of these carbon atoms^{11,12}, it is expected that these carbon atoms preferably react with the terminal alkyne carbon atoms in the cyclization. This is exactly what happens in the formation of the energetically most stable product **2a-trans2**. For **2a-cis**, on the other hand, only one of the alkyne groups forms a ring involving an olefinic carbon atom, while the other one attaches to a β -carbon within the aromatic pathway. For **2a-trans1**, the least favourable product, both extra rings involve carbon atoms within the aromatic pathway.

To connect the two perspectives, that is, the energetics based on DFT calculations and the intuitive chemical aromaticity interpretation, we turned towards a more quantitative assessment of aromaticity: the Harmonic Oscillator Model of Aromaticity (HOMA) index^{50,51}. The HOMA index is one of the most widespread measures of structural aspects of aromaticity, mostly due to its versatility and direct

chemical interpretation. The HOMA index measures the deviation of the observed bond lengths from the 'optimal' aromatic bond lengths. The normalized sum of the squared deviations is subtracted from 1, such that a HOMA index close to 1 is obtained for a strongly aromatic system (that is, with all bond lengths close to the optimal values); for the formal definition, see Methods. We choose the HOMA index because it is sensitive to geometrical changes induced by adsorption of the molecules, as opposed to topological aromaticity descriptors⁵²⁻⁵⁴. Also, it can be used to quantify the aromaticity of extended macrocyclic pathways, which is more difficult with nucleus-independent chemical shift calculations^{7,26}. We used the DFT-computed bond lengths to calculate the HOMA indices^{55,56}, because it is not feasible to accurately extract absolute or even relative bond lengths from the AFM measurements due to substantial distortions in the images⁵⁷⁻⁵⁹. The calculations confirm the two-fold symmetry of the aromatic system and reveal two types of pyrrole rings with different aromaticity, in accordance with the model introduced in Fig. 1 (for calculations of local pyrrolic aromaticity,

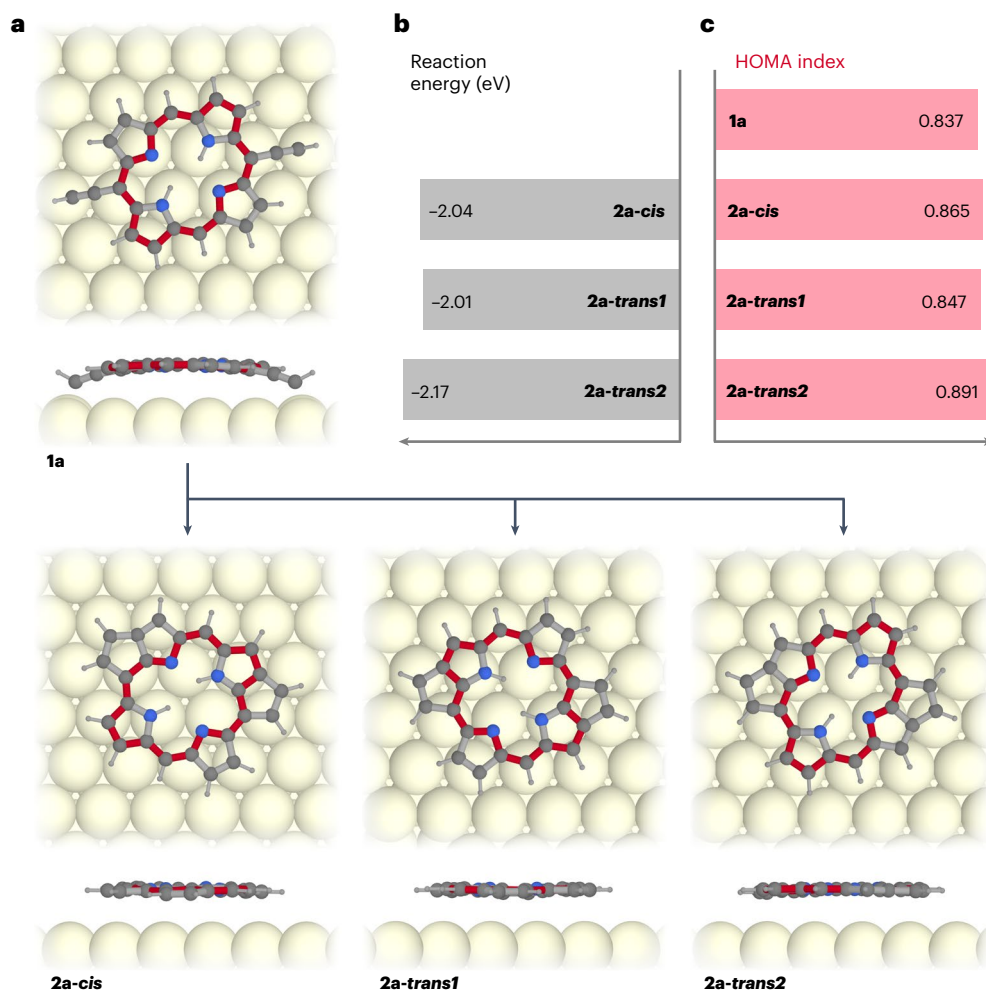


Fig. 4 | Correlation between aromaticity and thermodynamical stability. **a**, Top and side views of DFT relaxed structures of the precursor **1a** and the possible cyclization products: **2a-cis**, **2a-trans1** and **2a-trans2**. **2a-trans1** and **2a-trans2** correspond to different N–H tautomers (that is, different configuration of the inner hydrogen atoms). The red bonds mark the aromatic 18 π -electron diaza[18]annulene pathway in the structures. Colour code: grey, carbon; light grey, hydrogen; blue, nitrogen. **b**, DFT calculations of the reaction energies show that the energetically preferred product is **2a-trans2**, which is formed via

the cyclization reaction with the porphyrin β -carbons outside of the aromatic diaza[18]annulene pathway. On the other hand, **2a-trans1**, which is formed via cyclization with β -carbons within the aromatic pathway, is the least preferred product. **c**, The HOMA-aromaticity indices for the respective cyclization products show the same trend (that is, **2a-trans2** has the highest HOMA index, **2a-trans1** the lowest), substantiating the effect of aromaticity on the regioselectivity of the cyclization reaction.

see Supplementary Extended Data Fig. 4). Figure 4c shows the HOMA values associated with the macrocyclic diaza[18]annulene aromatic pathways for the reactant (**1a**) as well as for the three products (**2a-cis**, **2a-trans1** and **2a-trans2**). Strikingly, the HOMA values correlate with the DFT-calculated reaction energies (Fig. 4b): the highest aromaticity index is obtained for the energetically most favourable product (**2a-trans2**), while the product with the lowest HOMA index is also the energetically least preferred (**2a-trans1**).

Thus, all three perspectives, that is, the energetics based on DFT, the qualitative chemical intuitive picture, as well as the quantitative assessment of aromaticity, are in agreement—and importantly, also match the experimentally observed relative abundance of cyclization products (for estimates of predicted product abundances, see Supplementary Fig. 18). However, two important aspects warrant further discussion. These concern (1) the role of the substrate and (2) the role of the adjacent molecules on the energetics of the cyclization reaction.

To shed light on the influence of the substrate, we performed calculations for the products (**2a-cis**, **2a-trans1** and **2a-trans2**) at different adsorption sites. The reaction energies for one product at

different adsorption sites can vary by up to 0.1 eV (Fig. 5a). This variation reflects different adsorption energies of the respective molecules on the substrate (Fig. 5b). And while this variation is on the same order of magnitude as the variation of reaction energies between the different products, our initial conclusions remain unchanged: for all investigated adsorption positions the product **2a-trans2** is energetically preferred over the other two products (**2a-cis** and **2a-trans1**). The same trend holds true for the reaction of free-standing molecules, that is, without the substrate (dashed lines in Fig. 5).

Figure 5c shows that the variation of the calculated HOMA indices for one product at different adsorption sites is much smaller than the variation between the different products. This suggests that the aromaticity is not noticeably altered for different adsorption configurations. However, our calculations reveal that the HOMA indices for the surface-adsorbed species typically are slightly lower than for their free-standing counterparts. This can be explained by a small perturbation of the atom positions upon adsorption of the molecules on the substrate, inducing additional deviations of the bond lengths from their ‘optimal’ aromatic lengths. In addition, charge transfer between

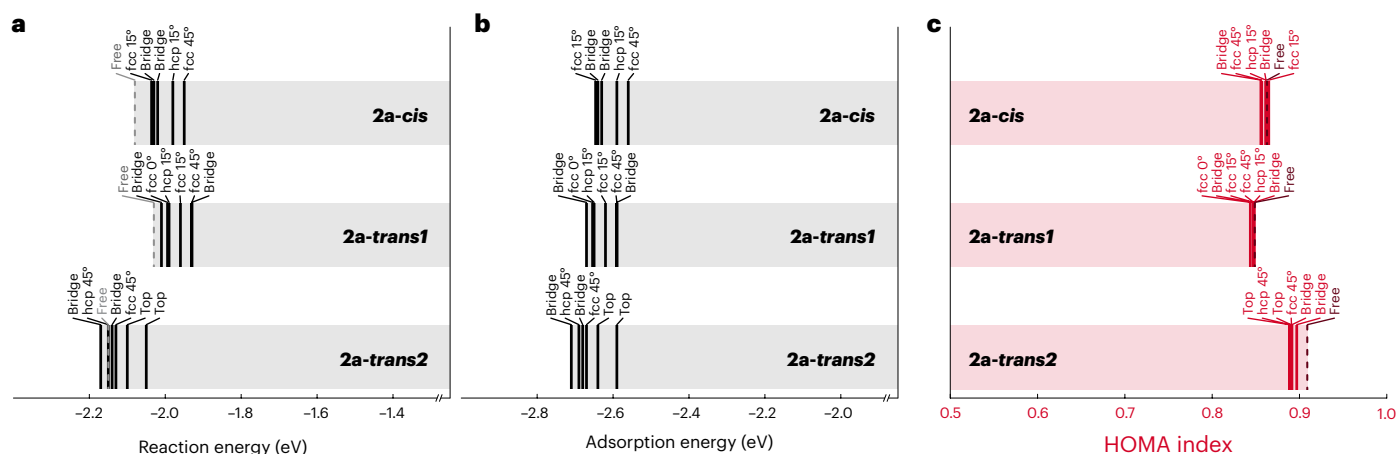


Fig. 5 | Influence of different adsorption positions. a–c. The graphs show the variation of reaction energies (a), adsorption energies (b) and HOMA indices (c) of the products **2a-cis**, **2a-trans1** and **2a-trans2** as a function of their adsorption configurations. Each vertical line marks one adsorption position, free-standing configurations are denoted by dashed lines (Extended Data Fig. 3 shows the respective structures and values in detail). The notable variation of

the adsorption energies for each molecule is reflected in the respective reaction energies. Nevertheless, the energetic preference for **2a-trans2** is not changed by the Au(111) substrate; it remains the most stable product for all investigated adsorption configurations. Adsorption typically decreases the HOMA index compared with the free-standing molecules (dashed lines), but only a rather small variation is observed for different adsorption sites.

the molecule and the substrate can play a role here (for an analysis of charge transfer, see Supplementary Fig. 19).

Most of our explanations regarding the cyclization were based on the understanding of single molecules. It is conceivable that the cyclization is influenced by the coupling reaction (which occurs at similar temperatures), as well as by non-covalent interactions with nearby molecules (molecular aggregates can even form for diluted surface concentrations). Due to computational complexity, it was not feasible to perform calculations that thoroughly investigate these effects. But the statistical analysis of our experiments indicates that coupling does not change the regioselectivity of the cyclization: both the coupled as well as the isolated molecules show the same preference for *trans*-cyclization. Non-covalent interactions within molecular aggregates will probably ‘push’ the molecules away from their most stable positions on the substrate (the same is expected to happen at elevated temperatures). And while changes of adsorption positions do not significantly alter the HOMA indices, they do have a noticeable effect on the reaction energies (Fig. 5). But, based on the calculations, this effect is unlikely to change the trends in reaction energies for the different products.

The cyclization reaction might also be influenced by other parameters that our models do not capture, such as steric effects or energy dissipation to the substrate²². But as the pathways towards *cis*- and *trans*-cyclized species are similar, such effects would very likely influence these pathways in a similar way and therefore would not lead to a notable preference for one of the products. Thus, despite such potential complexities, we believe that our theoretical models adequately describe the reaction and therefore correctly explain the pronounced preference of *trans*-cyclized species that has been experimentally observed for both isolated as well as coupled molecules. Beyond that, the reduced reactivity of aromatic β -carbons can directly explain the product distributions observed in previous studies of planarization reactions of tetraphenyl-porphyrins, which report comparable preferences for certain isomers^{60–62}.

Reaction kinetics

Finally, we closely examine and model the reaction kinetics. The transformation of **1a** involves two cyclization steps with two possibilities for each (Fig. 6c,d): formation of bonds with β -carbon atoms at the porphyrin periphery that are either within or outside of the aromatic

pathway. The first cyclization yields the half-cyclized intermediates **2a-pre1** and **2a-pre2**. These then can transform into **2a-trans1** and **2a-cis1**, as well as **2a-cis2** and **2a-trans2**. Note that **2a-cis1** and **2a-cis2** are equivalent structures (that can be seen as mirror images of each other), but they emerge from different reaction pathways and thus are distinguishable in this analysis. DFT-calculated reaction barriers for all four possible pathways show that the coupling steps with aromatically stabilized carbon atoms have higher barriers by up to 0.3 eV (Supplementary Figs 9–12). Considering the multiple steps for each transformation, we use the calculated barriers to simulate the reaction kinetics by solving the system of rate equations associated with the pathways shown in Fig. 6c. The simulations confirm the preference for the pathway towards **2a-trans2** (Fig. 6c). Furthermore, a pronounced dependence on the heating rate is revealed (Fig. 6b): the slower the heating rate, the stronger the preference for the reaction path towards **2a-trans2**. This can be intuitively explained by considering that with faster heating rates a wider energy range is accessed earlier in the reaction progress, which helps to overcome the reaction barriers associated with less preferred pathways. Following these predictions, we have conducted experiments with different temperature programmes (Fig. 6a). The experiments show a higher yield of *trans*-cyclized species and a stronger dependence on the heating ramp than the simulations. However, both experiment and simulation (Fig. 6a,b, respectively) reveal the same trend: slower heating rates increase the *trans*-cyclized product yields, clearly demonstrating the existence and prospects of kinetic reaction control.

Conclusion

We found that the concept of aromaticity can correctly predict the on-surface reactivity of porphyrinoid molecules. The aromatic diaza[18]annulene pathway of free-base porphyrins explains the regioselectivity of the cyclization reactions and thus the strong preference for *trans*-cyclization products. These observations agree with theoretical estimates of reaction energy differences on the order of 100 meV. The reaction energies of the products are directly correlated with their aromaticity as determined by calculation of their HOMA indices, which were found to be robust against adsorption on the substrate. Our results show that the predictive power of chemical reasoning based on the concept of aromaticity can be extended to on-surface chemistry—and can directly explain preferences for porphyrin cyclization pathways

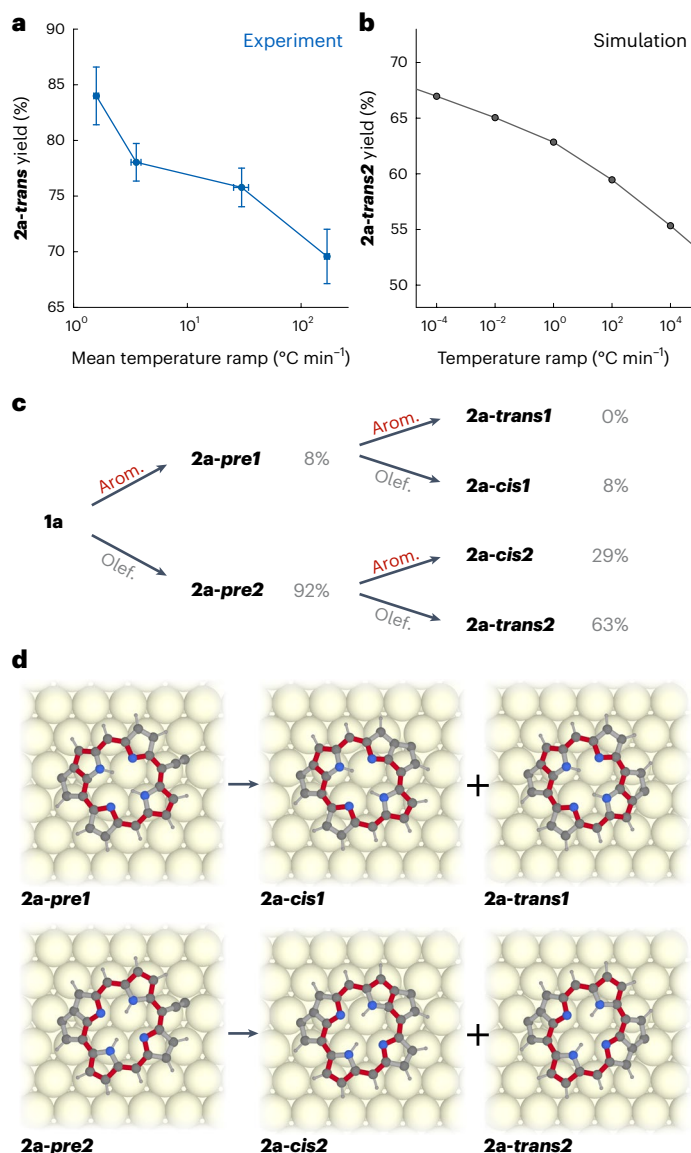


Fig. 6 | Reaction kinetics. **a**, Experimental yield of *trans*-cyclized species as a function of the average heating ramp (final annealing temperature of 305 °C). Slower ramps lead to a higher selectivity of the reaction. Error bars for the **2a-trans** yield represent the standard deviation based on the counting statistics (the total number of counted molecules for each datapoint were 200, 601, 611 and 355, respectively). Error bars for the temperature ramp estimate the experimental uncertainty. **b**, Kinetic simulations based on DFT-calculated reaction barriers show a similar trend of an increasing yield of **2a-trans2** with a slower annealing ramp. **c**, Scheme of the cyclization cascade of **1a** towards the half-cyclized intermediates **2a-pre1** and **2a-pre2** and the products **2a-trans1**, **2a-cis1**, **2a-cis2** and **2a-trans2**. Both cyclization steps preferentially occur at the olefinic β -carbon atoms at the porphyrin periphery (that is, the pathways labelled 'olef.'). The calculated yields of intermediates and products with respect to the precursor **1a** are given for a heating ramp of 1 °C min⁻¹. **d**, Structural models of the DFT-relaxed intermediates and products.

in previous studies^{60–62}. These insights can help to guide the design of precursors for controlled synthesis of surface-supported molecular nanoarchitectures with specific morphologies and functions.

References

- Krygowski, T. M., Cyrański, M. K., Czarnocki, Z., Häfeli, G. & Katritzky, A. R. Aromaticity: a theoretical concept of immense practical importance. *Tetrahedron* **56**, 1783–1796 (2000).
- Ragué Schleyer, P. V. Introduction: aromaticity. *Chem. Rev.* **101**, 1115–1117 (2001).
- Minkin, V. I. Glossary of terms used in theoretical organic chemistry. *Pure Appl. Chem.* **71**, 1919–1981 (1999).
- Hückel, E. Quantentheoretische Beiträge zum Benzolproblem. *Z. Phys.* **70**, 204–286 (1931).
- Vogel, E., Köcher, M., Schmickler, H. & Lex, J. Porphycene—a novel porphyrin isomer. *Angew. Chem. Int. Ed. Engl.* **25**, 257–259 (1986).
- Vogel, E. The porphyrins from the 'annulene chemist's' perspective. *Pure Appl. Chem.* **65**, 143–152 (1993).
- Wu, J. I., Fernández, I. & Schleyer, P. V. R. Description of aromaticity in porphyrinoids. *J. Am. Chem. Soc.* **135**, 315–321 (2013).
- Vogel, E. From small carbocyclic rings to porphyrins: a personal account of 50 years of research. *Angew. Chem. Int. Ed.* **50**, 4278–4287 (2011).
- Solov'ev, K. N., Mashenkov, V. A., Gradyushko, A. T., Turkova, A. E. & Lezina, V. P. High resolution NMR spectra of porphin and of porphin derivatives. *J. Appl. Spectrosc.* **13**, 1106–1111 (1970).
- Scheer, H. & Katz, J. J. in *Porphyrins and Metalloporphyrins* (ed Smith, K. M.) 399–524 (Elsevier, 1975).
- Brückner, C. The breaking and mending of meso-tetraarylporphyrins: transmuting the pyrrolic building blocks. *Acc. Chem. Res.* **49**, 1080–1092 (2016).
- Senge, M. O., Sergeeva, N. N. & Hale, K. J. Classic highlights in porphyrin and porphyrinoid total synthesis and biosynthesis. *Chem. Soc. Rev.* **50**, 4730–4789 (2021).
- Pavliček, N. et al. Synthesis and characterization of triangulene. *Nat. Nanotechnol.* **12**, 308–311 (2017).
- Wang, X. Y. et al. Exploration of pyrazine-embedded antiaromatic polycyclic hydrocarbons generated by solution and on-surface azomethine ylide homocoupling. *Nat. Commun.* **8**, 1–7 (2017).
- Majzik, Z. et al. Studying an antiaromatic polycyclic hydrocarbon adsorbed on different surfaces. *Nat. Commun.* **9**, 1–6 (2018).
- Di Giovannantonio, M. et al. On-surface synthesis of antiaromatic and open-shell indeno[2,1-b]fluorene polymers and their lateral fusion into porous ribbons. *J. Am. Chem. Soc.* **141**, 12346–12354 (2019).
- Kawai, S. et al. Competing annulene and radialene structures in a single anti-aromatic molecule studied by high-resolution atomic force microscopy. *ACS Nano* **11**, 8122–8130 (2017).
- Zuzak, R., Stoica, O., Blicek, R., Echavarren, A. M. & Godlewski, S. On-surface synthesis and intermolecular cycloadditions of indacenoditetracenes, antiaromatic analogues of undecacene. *ACS Nano* **15**, 1548–1554 (2021).
- Fatayer, S. et al. Molecular structure elucidation with charge-state control. *Science* **365**, 142–145 (2019).
- Cai, J. et al. Atomically precise bottom-up fabrication of graphene nanoribbons. *Nature* **466**, 470–473 (2010).
- Clair, S. & De Oteyza, D. G. Controlling a chemical coupling reaction on a surface: tools and strategies for on-surface synthesis. *Chem. Rev.* **119**, 4717–4776 (2019).
- Riss, A. et al. Imaging single-molecule reaction intermediates stabilized by surface dissipation and entropy. *Nat. Chem.* **8**, 678–683 (2016).
- Grill, L. et al. Nano-architectures by covalent assembly of molecular building blocks. *Nat. Nanotechnol.* **2**, 687–691 (2007).

24. Mallada, B. et al. On-surface synthesis of one-dimensional coordination polymers with tailored magnetic anisotropy. *ACS Appl. Mater. Interf.* **13**, 32393–32401 (2021).
25. Saywell, A., Browning, A. S., Rahe, P., Anderson, H. L. & Beton, P. H. Organisation and ordering of 1D porphyrin polymers synthesised by on-surface Glaser coupling. *Chem. Commun.* **52**, 10342–10345 (2016).
26. Seufert, K. et al. Porphine homocoupling on Au(111). *J. Phys. Chem. C* **123**, 16690–16698 (2019).
27. Wiengarten, A. et al. Surface-assisted dehydrogenative homocoupling of porphine molecules. *J. Am. Chem. Soc.* **136**, 9346–9354 (2014).
28. Sun, Q. et al. Bottom-up fabrication and atomic-scale characterization of triply linked, laterally π -extended porphyrin nanotapes. *Angew. Chem. Int. Ed.* **60**, 16208–16214 (2021).
29. Auwärter, W., Ācija, D., Klappenberger, F. & Barth, J. V. Porphyrins at interfaces. *Nat. Chem.* **7**, 105–120 (2015).
30. Bischoff, F. et al. Exploration of interfacial porphine coupling schemes and hybrid systems by bond-resolved scanning probe microscopy. *Angew. Chem. Int. Ed.* **57**, 16030–16035 (2018).
31. Chen, S. et al. On-surface synthesis of 2D porphyrin-based covalent organic frameworks using terminal alkynes. *Chem. Mater.* **33**, 8677–8684 (2021).
32. Yue, J. Y., Liu, X. H., Sun, B. & Wang, D. The on-surface synthesis of imine-based covalent organic frameworks with non-aromatic linkage. *Chem. Commun.* **51**, 14318–14321 (2015).
33. Meng, X. et al. Effect of central π -system in silylated-tetraynes on σ -bond metathesis on surfaces. *J. Phys. Chem. C* **122**, 6230–6235 (2018).
34. Riss, A. et al. Polycyclic aromatic chains on metals and insulating layers by repetitive [3+2] cycloadditions. *Nat. Commun.* **11**, 1–8 (2020).
35. Kawai, S. et al. Diacetylene linked anthracene oligomers synthesized by one-shot homocoupling of trimethylsilyl on Cu(111). *ACS Nano* **12**, 8791–8797 (2018).
36. Zhang, L. et al. On-surface activation of trimethylsilyl-terminated alkynes on coinage metal surfaces. *ChemPhysChem* **20**, 2382–2393 (2019).
37. Gross, L., Mohn, F., Moll, N., Liljeroth, P. & Meyer, G. The chemical structure of a molecule resolved by atomic force microscopy. *Science* **325**, 1110–1114 (2009).
38. Riss, A. et al. Local electronic and chemical structure of oligo-acetylene derivatives formed through radical cyclizations at a surface. *Nano Lett.* **14**, 2251–2255 (2014).
39. Schuler, B. et al. Adsorption geometry determination of single molecules by atomic force microscopy. *Phys. Rev. Lett.* **111**, 106103 (2013).
40. Albrecht, F., Bischoff, F., Auwärter, W., Barth, J. V. & Repp, J. Direct identification and determination of conformational response in adsorbed individual nonplanar molecular species using noncontact atomic force microscopy. *Nano Lett.* **16**, 7703–7709 (2016).
41. Schwarz, M. et al. Corrugation in the weakly interacting hexagonal-BN/Cu(111) system: Structure determination by combining noncontact atomic force microscopy and X-ray standing waves. *ACS Nano* **11**, 9151–9161 (2017).
42. Braun, J. et al. NMR study of the tautomerism of porphyrin including the kinetic HH/HD/DD isotope effects in the liquid and the solid state. *J. Am. Chem. Soc.* **116**, 6593–6604 (1994).
43. Schlabach, M., Rumpel, H. & Limbach, H.-H. Investigation of the tautomerism of ^{15}N -labeled hydroporphyrins by dynamic NMR spectroscopy. *Angew. Chemie Int. Ed. Engl.* **28**, 76–79 (1989).
44. Liljeroth, P., Repp, J. & Meyer, G. Current-induced hydrogen tautomerization and conductance switching of naphthalocyanine molecules. *Science* **317**, 1203–1206 (2007).
45. Auwärter, W. et al. A surface-anchored molecular four-level conductance switch based on single proton transfer. *Nat. Nanotechnol.* **7**, 41–46 (2011).
46. Bischoff, F. et al. How surface bonding and repulsive interactions cause phase transformations: ordering of a prototype macrocyclic compound on Ag(111). *ACS Nano* **7**, 3139–3149 (2013).
47. Schlabach, M. et al. NMR and NIR studies of the tautomerism of 5,10,15,20-tetraphenylporphyrin including kinetic HH/HD/DD isotope and solid state effects. *Ber. Bunsenges. Phys. Chem.* **96**, 821–833 (1992).
48. Storm, C. B. & Teklu, Y. Nitrogen-hydrogen tautomerism in porphyrines and chlorines. *J. Am. Chem. Soc.* **3939**, 1745–1747 (1970).
49. Claramunt, R. M., Elguero, J. & Katritzky, A. R. Tautomerism involving other than five- and six-membered rings. *Adv. Heterocycl. Chem.* **77**, 1–50 (2000).
50. Kruszewski, J. & Krygowski, T. M. Definition of aromaticity basing on the harmonic oscillator model. *Tetrahedron Lett.* **13**, 3839–3842 (1972).
51. Krygowski, T. M., Szatyłowicz, H., Stasyuk, O. A., Dominikowska, J. & Palusiak, M. Aromaticity from the viewpoint of molecular geometry: application to planar systems. *Chem. Rev.* **114**, 6383–6422 (2014).
52. Krygowski, T. M. & Cyrński, M. K. Structural aspects of aromaticity. *Chem. Rev.* **101**, 1385–1419 (2001).
53. Garcia-Borrás, M., Osuna, S., Luis, J. M., Swart, M. & Solà, M. The role of aromaticity in determining the molecular structure and reactivity of (endohedral metallo) fullerenes. *Chem. Soc. Rev.* **43**, 5089–5105 (2014).
54. Yu, D. et al. Global and local aromaticity of acenes from the information-theoretic approach in density functional reactivity theory. *Phys. Chem. Chem. Phys.* **21**, 18195–18210 (2019).
55. Radula-Janik, K., Kopka, K., Kupka, T. & Ejsmont, K. Substituent effect of nitro group on aromaticity of carbazole rings. *Chem. Heterocycl. Compd.* **50**, 1244–1251 (2014).
56. Frizzo, C. P. & Martins, M. A. P. Aromaticity in heterocycles: new HOMA index parametrization. *Struct. Chem.* **23**, 375–380 (2011).
57. Gross, L. et al. Bond-order discrimination by atomic force microscopy. *Science* **337**, 1326–1329 (2012).
58. Hapala, P. et al. Mechanism of high-resolution STM/AFM imaging with functionalized tips. *Phys. Rev. B* **90**, 085421 (2014).
59. Hapala, P., Temirov, R., Tautz, F. S. & Jelínek, P. Origin of high-resolution IETS-STM images of organic molecules with functionalized tips. *Phys. Rev. Lett.* **113**, 226101 (2014).
60. Bischoff, F. et al. Surface-mediated ring-opening and porphyrin deconstruction via conformational distortion. *J. Am. Chem. Soc.* **143**, 15131–15138 (2021).
61. Lu, J. et al. Identification and electronic characterization of four cyclodehydrogenation products of H2TPP molecules on Au(111). *Phys. Chem. Chem. Phys.* **23**, 11784–11788 (2021).
62. Wiengarten, A. et al. Surface-assisted cyclodehydrogenation; break the symmetry, enhance the selectivity. *Chemistry* **21**, 12285–12290 (2015).

Methods

Sample preparation

The Au(111) single crystal substrate was cleaned via cycles of Ar⁺ sputtering and annealing up to 400 °C. Precursors 5,15-*bis*(trimethylsilyl)ethynylporphyrin (**1a**) and (5,15-*bis*(trimethylsilyl)ethynylporphyrinato) copper(II) (**1b**) were deposited from a quartz crucible (at sublimation temperatures of 250 °C for **1a** and 270 °C for **1b**) onto the substrates held at room temperature. The deposition time was appropriately controlled to obtain a molecular coverage of ~25% of a full layer. Upon annealing the substrate at 305 °C for 10 min, both **1a** and **1b** formed into one-dimensional porphyrin nanostructures, denoted by **2a** and **2b**, respectively. To investigate reaction kinetics, we used different heating programmes: (1) heating directly to 305 °C at a rate of 170 °C min⁻¹, (2) heating directly to 305 °C at a rate of 30 °C min⁻¹, (3) stepwise heating to 305 °C (200 °C to 245 °C for 10 min, 245 °C for 10 min, 245 °C to 275 °C for 10 min, 275 °C for 10 min and 275 °C to 305 °C for 10 min), (4) stepwise heating to 305 °C (180 °C for 10 min, 205 °C for 40 min, and 225 °C, 245 °C, 275 °C and 305 °C for 10 min at each temperature). The average temperature ramp (as plotted in Fig. 6a) was calculated for temperatures above 100 °C.

STM and AFM measurements

All STM/AFM measurements were performed with a commercial instrument (CreaTec) at 5 K and a base pressure below 4 × 10⁻¹⁰ mbar. STM images were recorded in constant current mode. The scanning parameters (tunnelling current *I*, and sample bias *V*_s) are given in the respective figure captions. Bond-resolved AFM measurements were acquired at constant height and *V*_s = 0 V using a qPlus tuning fork sensor⁶³ (resonance frequency ~31 kHz, oscillation amplitude 60 pm, *Q* value >100,000, stiffness *k* ≈ 1,800 Nm⁻¹) operated in frequency modulation mode. The measurements were performed with CO-terminated tips^{37,64}, obtained by vertical manipulation of adsorbed CO molecules that were dosed onto the substrate at *T* < 10 K. The data were analysed using SpmImage Tycoon⁶⁵.

DFT calculations

The calculations were performed in the DFT framework using the Vienna ab-initio simulation package (VASP)⁶⁶. The projector-augmented wave method was used to describe the interactions between ions and electrons⁶⁷. The exchange–correlation interactions were treated by van der Waals density functional (vdWDF) in the version of rev-vdWDF2 proposed by Hamada⁶⁸. Plane waves were used as a basis set with an energy cut-off of 400 eV. In all calculations, a *p*(8 × 8) surface unit cell was used and the first Brillouin zone was sampled by the gamma point only. The atomic structures were relaxed until the energy was less than 10⁻⁶ eV and the residual forces on all unconstrained atoms were less than 0.01 eV Å⁻¹. The Au(111) substrate was modelled by four-layered slabs separated by a 15 Å vacuum region for the structural models, where the bottom two layers were fixed. The reaction energies were obtained by calculating the energy difference between the cyclization products (**2a-cis**, **2a-trans1** and **2a-trans2**) and the corresponding precursor (**1a**). The transition states were searched by a combination of Climbing Image Nudge Elastic Band method and Dimer method^{69–71}. Charge transfer values were obtained by Bader charge analysis⁷².

HOMA index

The HOMA^{50,51} is defined as:

$$\text{HOMA} = 1 - \frac{1}{n} \sum_i^n V(d_{\text{opt}} - d_i)^2$$

Here, *n* is the number of bonds in aromatic pathway, *V* is a normalization constant (257.7 Å⁻² for C–C bonds and 93.52 Å⁻² for C–N bonds), *d*_{*i*} is the respective bond length and *d*_{opt} is the ‘optimal’ aromatic bond length^{51,55}. We determined the optimal aromatic bond lengths from the average DFT-computed C–C and C–N bond lengths in benzene and

pyrrole, respectively: 1.396 Å for C–C bonds and 1.375 Å for C–N bonds. For a perfectly aromatic system (that is, all bond lengths are equal to the ‘optimal’ aromatic bond lengths), a HOMA index of 1 is obtained.

Kinetic simulations

Kinetic simulations were performed by solving the system of rate equations for the transformation of **1a** as shown in Fig. 6c, using an instant thermalization approximation without taking entropic effects into account²².

Data availability

The data that support the findings are included in this published article (and its supplementary information files). Source data are provided with this paper. Source data for the graphs (Figs. 5 and 6a,b and Supplementary Figs. 9–17), DFT-optimized geometries (used in Figs. 4 and 5, Extended Data Figs. 3 and 4, and Supplementary Figs. 8–17, 20 and 22), and Bader charge analysis data (used in Supplementary Fig. 19) are made available in a zip file. Any additional datasets (STM and AFM data) generated during and/or analysed during the current study are available from the corresponding authors on reasonable request.

Code availability

Apps and libraries used to analyse the data and to generate images were made available in open-source repositories (<https://github.com/alexriiss/SpmlImageTycoon.jl> and <https://github.com/alexriiss/ChemfilesViewer.jl>). Any other code generated during the current study is available from the corresponding authors on reasonable request.

References

- Giessibl, F. J. The qPlus sensor, a powerful core for the atomic force microscope. *Rev. Sci. Instrum.* **90**, 011101 (2019).
- Bartels, L., Meyer, G. & Rieder, K. H. Controlled vertical manipulation of single CO molecules with the scanning tunnelling microscope: a route to chemical contrast. *Appl. Phys. Lett.* **71**, 213–215 (1997).
- Riss, A. SpmlImage Tycoon: organize and analyze scanning probe microscopy data. *J. Open Source Softw.* **7**, 4644 (2022).
- Kresse, G. Efficient iterative schemes for ab initio total-energy calculations using a plane-wave basis set. *Phys. Rev. B* **54**, 11169–11186 (1996).
- Blöchl, P. E. Projector augmented-wave method. *Phys. Rev. B* **50**, 17953–17979 (1994).
- Hamada, I. Van der Waals density functional made accurate. *Phys. Rev. B* **89**, 121103 (2014).
- Henkelman, G. & Jonsson, H. A dimer method for finding saddle points on high dimensional potential surfaces using only first derivatives. *J. Chem. Phys.* **111**, 7010–7022 (1999).
- Henkelman, G. & Jonsson, H. Improved tangent estimate in the nudged elastic band method for finding minimum energy paths and saddle points. *J. Chem. Phys.* **113**, 9978–9985 (2000).
- Henkelman, G., Uberuaga, B. P. & Jonsson, H. A climbing image nudged elastic band method for finding saddle points and minimum energy paths. *J. Chem. Phys.* **113**, 9901–9904 (2000).
- Henkelman, G., Arnaldsson, A. & Jónsson, H. A fast and robust algorithm for Bader decomposition of charge density. *Comput. Mater. Sci.* **36**, 354–360 (2006).
- Sperl, A., Kröger, J. & Berndt, R. Controlled metalation of a single adsorbed phthalocyanine. *Angew. Chem.* **123**, 5406–5409 (2011).
- Pham, V. D. et al. Control of molecule–metal interaction by hydrogen manipulation in an organic molecule. *J. Phys. Chem. Lett.* **7**, 1416–1421 (2016).
- Cyrański, M. K., Krygowski, T. M., Wisiorowski, M., Van Eikema Hommes, N. J. R. & Ragué Schleyer, P. V. Global and local aromaticity in porphyrins: an analysis based on molecular geometries and nucleus-independent chemical shifts. *Angew. Chem. Int. Ed.* **37**, 177–180 (1998).

76. Islyaikin, M. K., Ferro, V. R. & García De La Vega, J. M. Aromaticity in tautomers of triazoleporphyrazine. *J. Chem. Soc. Perkin Trans.* **2**, 2104–2109 (2002).
77. Aihara, J. I., Kimura, E. & Krygowski, T. M. Aromatic conjugation pathways in porphyrins. *Bull. Chem. Soc. Jpn* **81**, 826–835 (2008).

Acknowledgements

This work was funded by the Deutsche Forschungsgemeinschaft (DFG, German Research Foundation)—453903355, 326785818, under Germany's Excellence Strategy—EXC 2089/1–390776260 (e-conversion), and a grant from the Irish Research Council (New Foundations, PorOrgMat), and the Guangdong Basic and Applied Basic Research Foundation (grant no. 2019A1515110819). N.C. acknowledges the support from China Scholarship Council (CSC). M.O.S. was supported by the Technical University of Munich—Institute for Advanced Study through a Hans Fischer Senior Fellowship and by Science Foundation Ireland (21/FFP-A/9469). J.B. acknowledges funding from the Swedish Research Council. The computations were enabled by resources provided by the National Academic Infrastructure for Supercomputing in Sweden (NAISS) and the Swedish National Infrastructure for Computing (SNIC) at the National Supercomputer Centre (NSC), partially funded by the Swedish Research Council through grant agreements no. 2022-06725 and no. 2018-05973. Funding for E.C.-R. was provided by CONACYT-Chihuahua, Mexico (Scholarship 591246). We kindly thank F. Klappenberger for his support during the initial project stage. The funders had no role in study design, data collection and analysis, decision to publish or preparation of the manuscript.

Author contributions

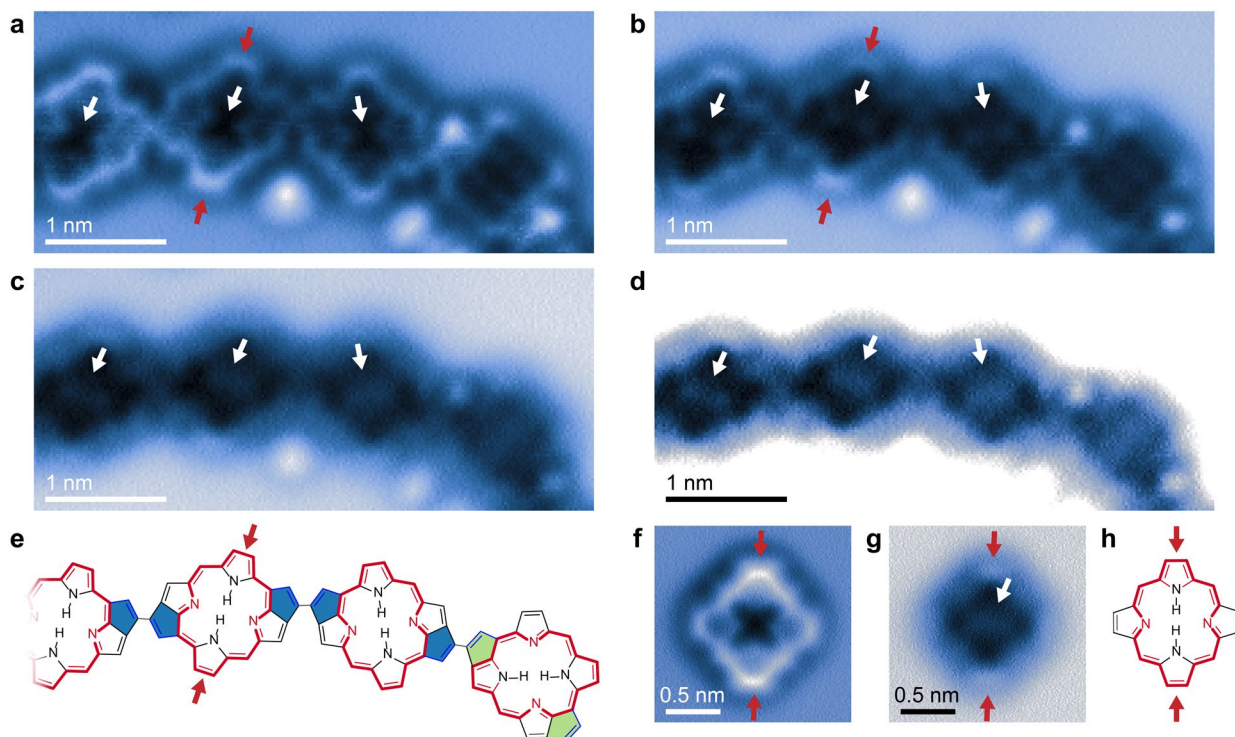
A.R. conceived the analysis. N.C and A.R. designed the experiments. N.C. performed the experiments and the DFT calculations. E.C.-R. helped with the experiments and interpretation. A.R. supervised the experiments and did the HOMA analysis. J.B. supervised the DFT calculations. Z.C. synthesized the precursors, supervised by M.R. M.O.S. provided insights and guidance for the chemical interpretation. J.V.B. provided materials and methods and supervised the project. N.C. and A.R. wrote the manuscript with help from all other authors.

Competing interests

The authors declare no competing interests.

Additional information

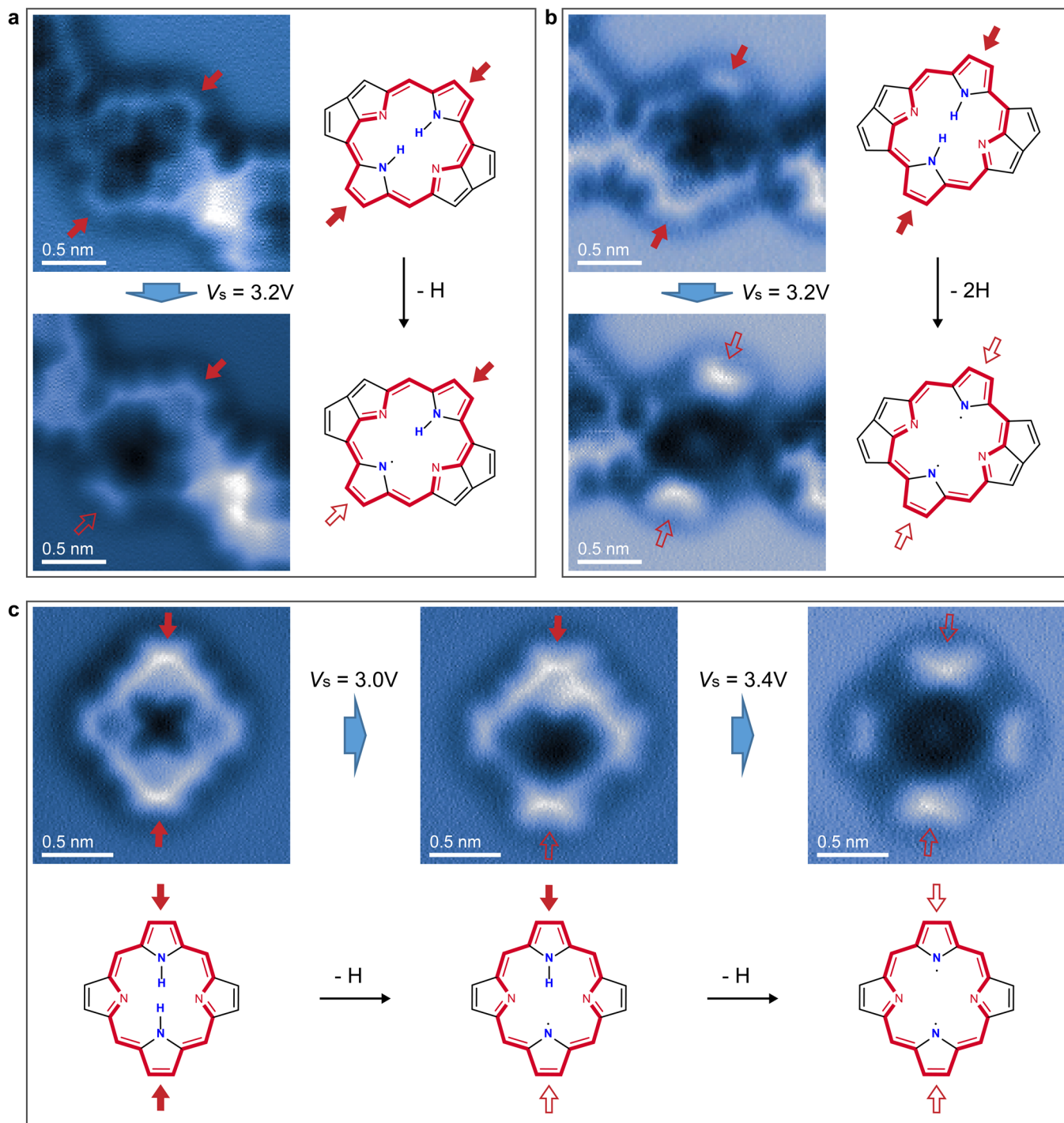
Correspondence and requests for materials should be addressed to Johannes V. Barth or Alexander Riss.



Extended Data Fig. 1 | Identification of hydrogen tautomers via AFM.

(a-c) AFM images of a chain of three *trans*-cyclized and one *cis*-cyclized molecule at different tip-sample distances. The *trans*-cyclized species show brighter features associated with one pair of nitrogen atoms at opposite sides, as marked by white arrows. (d) The same image as in (c), but with increased contrast. Such bright features connecting one pair of opposing nitrogen atoms were observed in previous work and assigned to iminic nitrogen atoms (Supplementary Fig. 6)¹⁹, *that is*, nitrogen atoms within the pyrrole rings that do not carry internal hydrogens. This assignment corresponds to the **2a-trans2** type. (e) Proposed chemical structure of the chain, consisting of three **2a-trans2** and one **2a-cis**

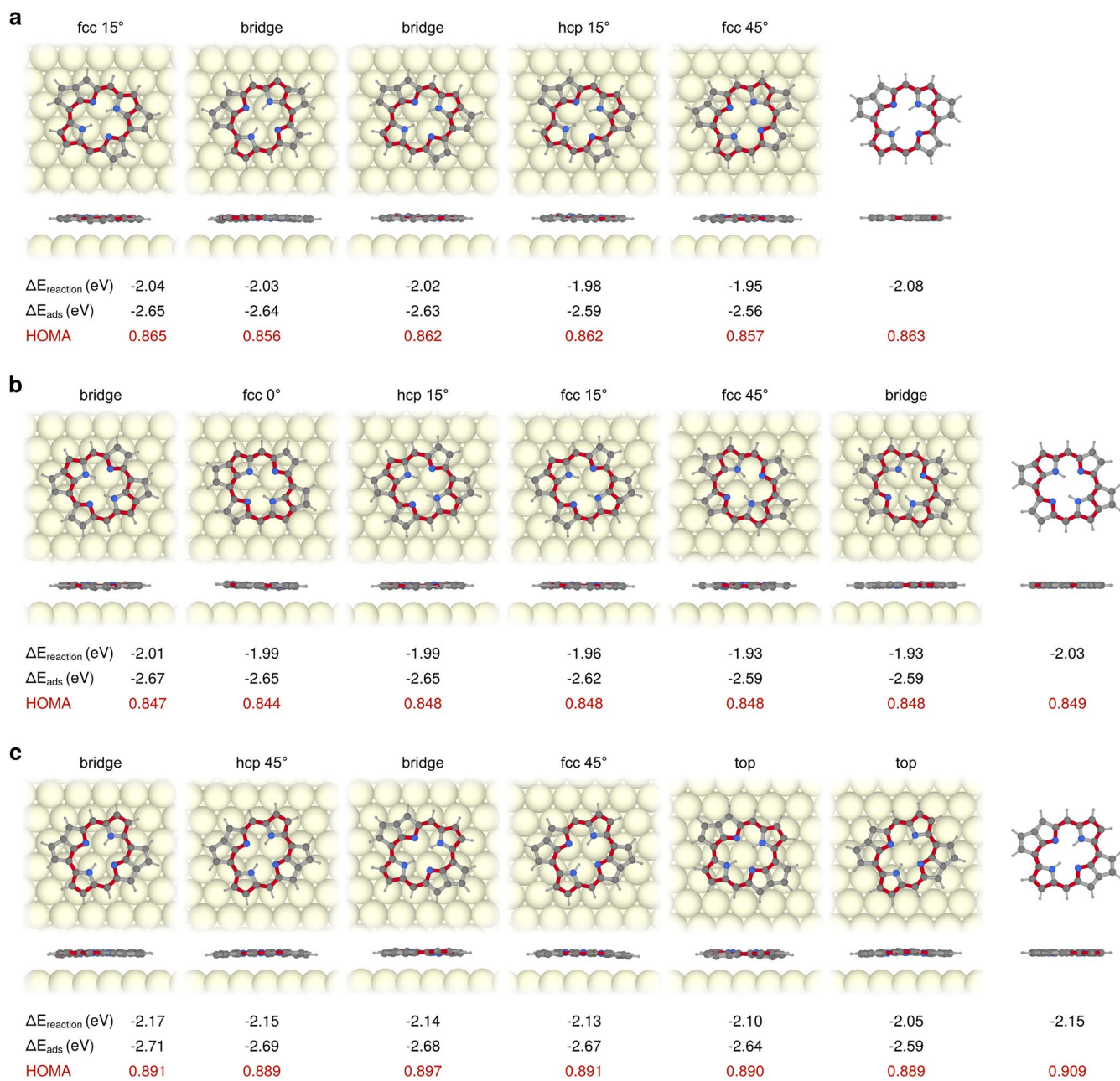
molecule. (f),(g) AFM images of an unsubstituted porphyrin molecule adsorbed on Au(111) shows similar features at larger tip-sample heights: a line along the direction of the iminic nitrogen atoms can be seen, marked by the white arrow. (h) Chemical structure of the molecule in (f) and (g). Red arrows mark aminic pyrroles. Scan parameters: $V_s = 0$ V, constant height. We have investigated 165 *trans*-cyclized molecules (see also Supplementary Fig. 5), all of which exhibit these particular features, suggesting that (almost) all of the *trans*-cyclized species are of type **2a-trans2**. Further support for this assignment is obtained by tip manipulation experiments (see Extended Data Fig. 2).



Extended Data Fig. 2 | Tip-induced cleavage of inner hydrogens.

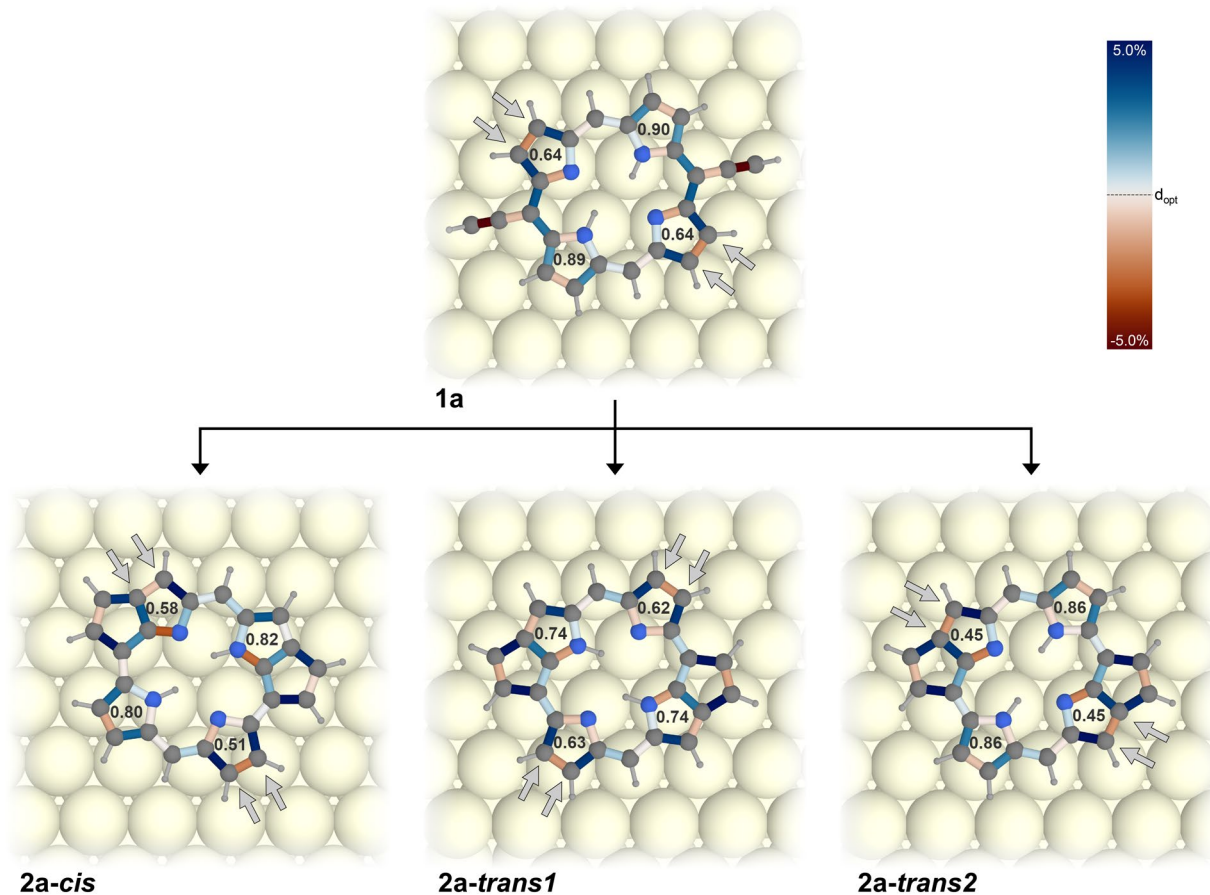
(a) Application of a voltage pulse ($V_s = 3.2\text{ V}$) close to the center of a *trans*-cyclized molecule within a chain leads to cleavage of an inner hydrogen atom^{45,73,74}. A substantial contrast change on the lower side can be observed, as marked by filled (before manipulation) and outlined (after manipulation) red arrows. Thus, we deduce that the pyrrole ring at this position was carrying one of the inner hydrogen atoms before the manipulation. This assignment corresponds to a *2a-trans2* type molecule. **(b)** A similar experiment (with a voltage pulse of $V_s = 3.2\text{ V}$) shows the cleavage of both inner hydrogen atoms, inducing contrast

changes at the top and bottom (marked by red arrows). Again, these positions are associated with the pyrroles that carry the inner hydrogen atoms, indicating that this molecule is of type *2a-trans2*. We have successfully performed such manipulation experiments on 10 molecules, all of which were confirmed to be of type *2a-trans2*. **(c)** Analogous experiments on unsubstituted porphyrin molecules adsorbed on Au(111). The two inner hydrogens can be cleaved off in two steps, both times associated with contrast changes at the respective hydrogen-carrying pyrrole rings (marked by red arrows). Scan parameters: $V_s = 0\text{ V}$, constant height.



Extended Data Fig. 3 | Relaxed geometries of the cyclization products. Top and side views of relaxed structures of (a) *2a-cis*, (b) *2a-trans1* and (c) *2a-trans2* at different adsorption positions, as well as in their free-standing geometry. For

each structure, the reaction energies (with respect to the model of the precursor **1a**), the adsorption energies, as well as the HOMA indices associated with the aromatic diaza[18]annulene pathway are shown.



Extended Data Fig. 4 | Local HOMA indices and relative bond lengths.

The images show the local HOMA indices for the pyrrole rings, as well as the relative bond lengths of each C-C and C-N bond (red for shortened and blue for elongated bond lengths, compared with the 'optimal' aromatic bond lengths ' d_{opt} '). The precursor **1a** exhibits an asymmetry, with one pair of two pyrrole rings at opposite 'corners' having higher HOMA indices than the other pair. This is in line with the aromatic diaza[18]annulene pathway (see Fig. 1 in the main text) observed in porphyrins⁷⁵⁻⁷⁷. The two pairs of carbon atoms with olefinic character outside of the aromatic pathway are marked by gray arrows. The cyclized

products also exhibit this twofold symmetry, but there are significant changes in the HOMA indices for the rings. The newly formed five-membered rings lead to a reduction of the HOMA indices of the pyrrole rings that they are attached to. For the structures **2a-cis**, **2a-trans1**, and **2a-trans2**, an additional 22 π -electron circuit exists along all the carbon atoms in the periphery of the molecules. The HOMA indices for these circuits are lower: 0.552 for **2a-cis**, 0.464 for **2a-trans1**, and 0.540 for **2a-trans2**. Furthermore, some of the atoms at the newly formed five-membered rings might be sp^3 -hybridized (see Supplementary Fig. 7), thus inhibiting conjugation along these 22 π -electron circuits.